Partial *k*-Space Reconstruction in Single-Shot Diffusion-Weighted Echo-Planar Imaging

Pippa Storey,[1,2*] Fred J. Frigo,[3] R. Scott Hinks,[3] Bryan J. Mock,[3] Bruce D. Collick,[3] Nicole Baker,[4] Jonathan Marmurek,[4,5] and Simon J. Graham[4,5]

Partial *k*-space sampling is frequently used in single-shot diffusion-weighted echo-planar imaging (DW-EPI) to reduce the TE and thereby improve the SNR. However, it increases the sensitivity of the technique to bulk rotational motion, which introduces a phase gradient across the tissue that shifts the echo in *k*-space. If the echo is displaced into the high spatial frequencies, conventional homodyne reconstruction fails, causing intensity oscillations across the image. Zero-padding, on the other hand, compromises the image resolution and may cause truncation artifacts. We present an adaptive version of the homodyne algorithm that detects the location of the echo in *k*-space and adjusts the center and width of the homodyne filters accordingly. The adaptive algorithm produces artifact-free images when the echo is shifted into the high positive *k*-space range, and reduces to the standard homodyne algorithm in the absence of bulk motion. Magn Reson Med 57: 614–619, 2007. © 2007 Wiley-Liss, Inc.

Key words: diffusion imaging; motion; signal loss partial *k*-space sampling; homodyne reconstruction

Diffusion-weighted imaging (DWI) is widely used in clinical neuroradiology to detect acute stroke and assess myelin development and integrity. It is typically implemented using a Stejskal-Tanner technique (1), which involves the application of strong magnetic field gradients. The gradients provide the necessary diffusion weighting, but they also render the signal extremely sensitive to pulsatile flow and bulk motion, such as head movement and table vibrations. Even very gentle motion produces large phase shifts in the emitted signal. Since any variation in motion between sampling periods would result in large phase inconsistencies among the data, most diffusion imaging sequences employ a single-shot readout, such as an echo-planar acquisition (2) or single-shot fast spin echo (SSFSE) (3). This prevents ghosting by ensuring that any motion-induced phase shifts will be consistent across the data set.

However, the use of an single-shot readout does not eliminate the effects of motion entirely. Rigid-body rotational motion during the application of the diffusion-sensitizing gradients introduces a linear phase shift across the tissue, which displaces the echo in *k*-space (4,5). If the rotational speed is sufficiently high, the DC component of the signal may be displaced outside the *k*-space sampling range, causing dramatic signal loss (6). We show that further complications arise with the use of partial *k*-space techniques, which are frequently employed in single-shot diffusion imaging to shorten the readout duration and minimize the TE. Standard reconstruction methods, such as the homodyne and Margosian algorithms (7,8), assume that any phase modulation across the tissue is slowly varying—a condition that can be violated in the presence of rotational motion. As we will demonstrate, failure of this condition causes image artifacts that are characterized by rapid intensity oscillations. The commonly used alternative of zero-padding the unsampled portion of *k*-space avoids these artifacts but reduces the image resolution and may cause Gibbs ringing due to data truncation. We propose instead an adaptive version of the homodyne algorithm, which incorporates sliding filters that adjust dynamically to the position of the echo in *k*-space.

THEORY

Diffusion-sensitizing gradient pulses are typically applied in balanced pairs, in combination with one or more refocusing RF pulses (2,9). Stationary spins are unaffected, but moving spins receive a velocity-dependent phase shift. In tissue with high rates of diffusion, the gradients cause dephasing among the spins. This produces a local reduction in signal and allows the formation of a DW image. Any coherent component in the motion will introduce a net phase shift into the emitted signal.

For a sequence with a single pair of diffusion-sensitizing gradient pulses bracketing a 180° RF pulse, the phase shift φ is given by

$$\varphi = \gamma \mathbf{v}.\mathbf{G}\delta_{dur}\Delta_{sep}, \qquad [1]$$

where $\mathbf{v}$ is the velocity of the spins, and γ is their gyromagnetic ratio (equal to 42.58 MHz/T for protons). $\mathbf{G}$ denotes the amplitude of the gradient pulses, δ_{dur} is their duration, and Δ_{sep} is the time interval separating their leading edges. For symmetric pulses with finite ramp times, δ_{dur} is measured from halfway up the attack ramp to halfway down the decay ramp.

[1]Radiology Department, Evanston Northwestern Healthcare, Evanston, Illinois, USA.

[2]Radiology Department, Northwestern University Feinberg School of Medicine, Chicago, Illinois, USA.

[3]GE Healthcare, Waukesha, Wisconsin, USA.

[4]Imaging Research, Sunnybrook Health Sciences Centre, Toronto, Ontario, Canada.

[5]Department of Medical Biophysics, University of Toronto, Toronto, Ontario, Canada.

Grant sponsors: Ontario Research and Development Challenge Fund; Natural Sciences and Engineering Research Council of Canada; GE Healthcare.

*Correspondence to: Pippa Storey, Radiology Department, Evanston Hospital, Walgreen Building, G507, 2650 Ridge Ave., Evanston, IL 60201. E-mail: pstorey@enh.org

Received 3 February 2006; revised 31 August 2006; accepted 6 October 2006.

DOI 10.1002/mrm.21132
Published online in Wiley InterScience (www.interscience.wiley.com).

The effect of rigid body motion during the application of diffusion-sensitizing gradients has been studied by other authors (4,5), but we will rederive their results briefly using the present notation. Rigid-body motion can be decomposed into rotational and translational components:

$$\mathbf{v}(\mathbf{r}) = \mathbf{\Omega}_{rot} \times \mathbf{r} + \mathbf{v}_{trans}, \quad [2]$$

where $\mathbf{\Omega}_{rot}$ is the angular velocity and $\mathbf{r}$ is the position of the tissue element. Because the velocity varies linearly with position, so does the resulting phase shift:

$$\varphi(\mathbf{r}) = \gamma[\mathbf{\Omega}_{rot} \times \mathbf{r} + \mathbf{v}_{trans}].\mathbf{G}\delta_{dur}\Delta_{sep}, \quad [3]$$

Rearranging this equation with the aid of a simple vector identity gives

$$\varphi(\mathbf{r}) = \gamma[(\mathbf{G} \times \mathbf{\Omega}_{rot}).\mathbf{r} + \mathbf{G}.\mathbf{v}_{trans}]\delta_{dur}\Delta_{sep}, \quad [4]$$

from which the phase gradient can be extracted:

$$\nabla\varphi = \gamma\mathbf{G} \times \mathbf{\Omega}_{rot}\delta_{dur}\Delta_{sep}, \quad [5]$$

A linear phase variation across the tissue, however, corresponds in general to a displacement of the data in *k*-space. This results from the Fourier relation between *k*-space and image space, and assumes that the image provides an accurate geometric representation of the tissue, i.e., that the readout introduces negligible distortion. Under this condition, the amplitude and direction of the *k*-space displacement $\Delta\mathbf{k}$ are given by the gradient of the phase modulation:

$$\Delta\mathbf{k} = \gamma\mathbf{G} \times \mathbf{\Omega}_{rot}\delta_{dur}\Delta_{sep}. \quad [6]$$

Note that the displacement in *k*-space is orthogonal to both the direction of the diffusion-sensitizing gradients and the axis of rotation. For example, if the rotation occurs within the imaging plane (e.g., side-to-side rolling during an axial acquisition), and the diffusion-sensitizing gradients are applied in the frequency-encoding direction *x*, then the echo will be shifted along the phase-encoding (PE) direction *y*, with a displacement given by

$$\Delta k_y = -\gamma\, G_x\Omega_z\delta_{dur}\Delta_{sep}. \quad [7]$$

In practice, *k*-space is sampled only over a limited range, which is determined by the desired resolution of the image. If Δk_y is sufficient to displace the DC component of the echo outside this range, the resulting image exhibits dramatic signal loss (6). This occurs if $|\Delta k_y| > k_{max}$, where $[-k_{max}, k_{max}]$ is the *k*-space sampling range. Since k_{max} is related to the image resolution δy through $k_{max} = \pi/\delta y$, the condition for signal loss can be interpreted as a phase change greater than π within a single voxel (6).

In partial *k*-space acquisitions, data are sampled only over the positive spatial frequencies plus a narrow band of low negative spatial frequencies, $[-k_0, k_{max}]$, where $k_0 \ll k_{max}$. By omitting most of the negative *k*-space lines, one can reduce the time taken to reach the center of *k*-space, and thereby shorten the TE and improve the SNR.

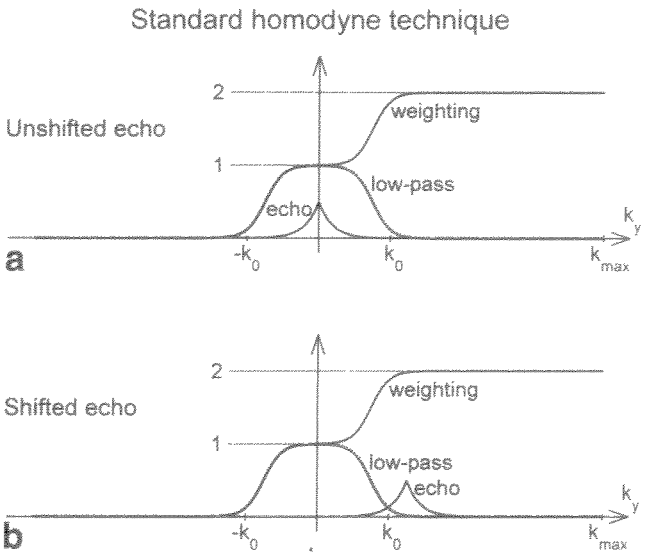

FIG. 1. Diagrams depicting the low-pass filter and weighting function used in standard homodyne reconstruction. The data are assumed to be sampled over the range $[-k_0, k_{max}]$. **a:** In the absence of motion, the echo is centered at $\mathbf{k} = 0$ and the low-pass filter provides an adequate estimate of the phase variation across the tissue. **b:** When the echo is shifted due to rotational motion, the method does not correctly account for the phase variation across the tissue.

However, the sensitivity of the sequence to motion is exacerbated because the *k*-space sampling range is reduced. Even a small displacement of the echo into the negative *k*-space range $\Delta k_y < -k_0$ will cause dramatic signal loss.

Furthermore, if conventional homodyne or Margosian methods (7,8) are used for image reconstruction, an equivalent displacement into the positive *k*-space range $\Delta k_y > k_0$ cannot be tolerated either. These algorithms assume that any phase modulation of the signal across the tissue is slowly varying, and therefore can be adequately captured within the low-order spatial frequencies $[-k_0, k_0]$. If the phase gradient imparted by the rotation is large enough to displace the echo into the high positive spatial frequency range, $\Delta k_y > k_0$, the assumption is violated. One can predict the effect on the image by considering the details of the homodyne reconstruction algorithm (7). In brief, the algorithm involves estimating the phase modulation of the signal over the tissue from a low-pass version of *k*-space, contained in the range $[-k_0, k_0]$ (see Fig. 1a). A Fourier transform is then performed on a filtered copy of the original data set, in which the high spatial frequencies are given twice the weighting of the central lines to compensate for the missing negative *k*-space lines. In image space, the transformed data are then multiplied by the complex conjugate of the slowly varying phase modulation as estimated earlier. The real part of the result is taken to produce an image. The method is accurate provided the phase of the signal does indeed vary slowly across the tissue. If the phase varies too rapidly, it cannot be correctly estimated from the low-pass version of *k*-space. This can happen if the echo has been displaced outside the central range of *k*-space (Fig. 1b). The multiplication step described above will then not adequately remove the phase

from the transformed data, and the resulting image will exhibit high-frequency intensity oscillations.

The angular velocities at which signal loss or intensity oscillations occur can be calculated from Eq. [7], and satisfy the relation

$$|\Omega_z| > \frac{k_0}{\gamma |G_x| \delta_{dur} \Delta_{sep}}. \quad [8]$$

By inserting typical values for the parameters, we can gauge the sensitivity of the technique to rotational motion. For b = 1000 s/mm^2, the gradient amplitude and timing parameters on state-of-the-art clinical scanners are of the order of G ≈ 40 mT/m, $\delta_{dur} \approx 21$ ms, and $\Delta_{sep} \approx 27$ ms. The value of k_0 is determined by the field of view (FOV), matrix size, and number of "overscans" (negative k-space lines). In DW-EPI of the brain, typical values for the FOV and matrix size are 24 cm and 128 × 128, respectively, giving $k_{max} \approx 267$ m^{-1}. With 16 overscans (the default value on GE systems) the readout samples of 5/8 of k-space, so $k_0 \approx 67$ m^{-1}. In this case, signal loss or intensity oscillations may occur at angular velocities as low as ~0.01 Hz (i.e., 4° s^{-1}), which corresponds to very gentle head motion.

The sensitivity to motion, however, is also affected by any image distortion introduced by the readout method. EPI is very sensitive to inhomogeneities in the static field B_0 due to its low effective bandwidth in the PE direction. Even small field inhomogeneities arising from magnetic susceptibility differences in the body are sufficient to cause substantial compression or stretching in the PE direction. We have shown that rotational motion introduces a linear phase shift across the tissue. In the presence of distortion, the image does not provide an accurate geometrical representation of the tissue, so the phase shift will not be linear across the image. In regions where the image is compressed, the phase gradient will be magnified, and in regions where it is stretched, the phase gradient will be diminished. We can infer that artifacts or signal loss will occur at lower rotational velocities in regions of compression than in regions of stretching.

Since the oscillatory artifacts result from a failure of the standard homodyne algorithm, one should be able to avoid them by using a zero-padding approach instead of homodyne reconstruction. However, zero-padding compromises the image resolution and may cause Gibbs ringing. We hypothesized that we could eliminate the motion artifacts without any loss of resolution or Gibbs ringing by adjusting the homodyne filters dynamically to the position of the echo, as illustrated in Fig. 2. In the following sections we will present the results of in vivo studies and phantom experiments designed to test the theory, and evaluate the performance of the adaptive homodyne algorithm.

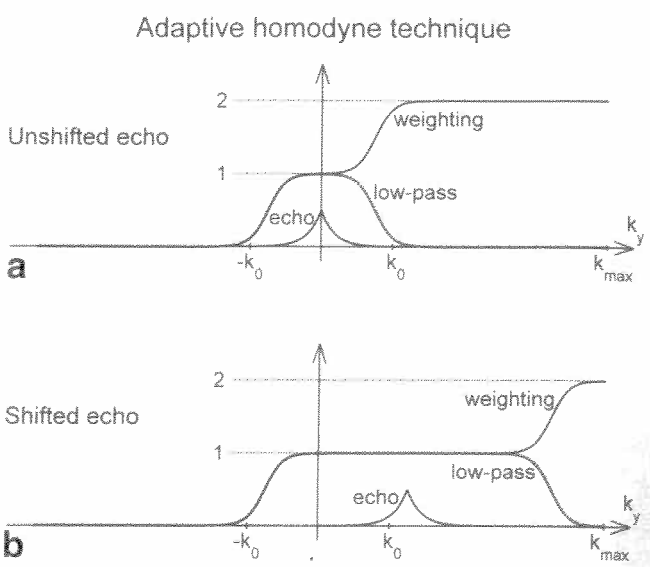

FIG. 2. Diagrams depicting the low-pass filter and weighting function for the adaptive homodyne algorithm. **a:** In the absence of motion, the method reduces to the standard homodyne algorithm (Fig. 1). **b:** When the echo is shifted due to rotational motion, the center and width of the low-pass filter and weighting function adjust accordingly to ensure that the phase variation across the tissue is correctly estimated.

MATERIALS AND METHODS

Human studies were conducted with the cooperation of two healthy volunteers who had provided informed consent in accordance with IRB requirements. The studies were performed on a 1.5T Signa Twinspeed system (GE Healthcare, Waukesha, WI, USA), using a quadrature birdcage head coil and a product DW-EPI sequence. With the subject lying supine and head-first in the scanner, an axial imaging slice was prescribed in the brain, with FOV = 24 cm, slice thickness = 8 mm, nominal matrix size = 128 × 128, bandwidth = 250 kHz, and TR = 1000 ms. Images were acquired with a b-value of 1000 s/mm^2 and diffusion-sensitizing gradients in three orthogonal directions (S/I, R/L and A/P). Other settings included the use of ramp sampling, partial k-space acquisition with 16 overscans (the default value on GE scanners), and PE in the A/P direction (to avoid nerve stimulation). The resulting TE was 69.4 ms. Each subject was asked to roll his head gently to the left or right during certain acquisitions. Images were generated using standard homodyne reconstruction (the default method on GE scanners). The filters used in the GE implementation of homodyne reconstruction are illustrated in Fig. 1. The raw data were also saved for analysis and further offline reconstruction.

Offline reconstruction with the zero-padding approach was performed using GE product software. In addition, an adaptive homodyne technique was implemented as illustrated in Fig. 2. The position of the echo along the PE direction was estimated automatically by finding the k-space data point with the highest magnitude. The center and width of the low-pass filter and weighting function were then adjusted accordingly.

Phantom experiments were performed on a 3.0T GE Healthcare system using a rotating phantom that consisted of a cube-shaped acrylic box containing plastic nuts and bolts, and Gd-DTPA-doped agar gel (10). It was mounted inside a quadrature birdcage head coil and rotated with the use of a stepper motor (Parker Hannifin Corp., USA) that was attached to the end of the patient bed and controlled from a console hosting LabVIEW 6 (National Instruments, Austin, TX, USA). The axis of rotation was parallel to that

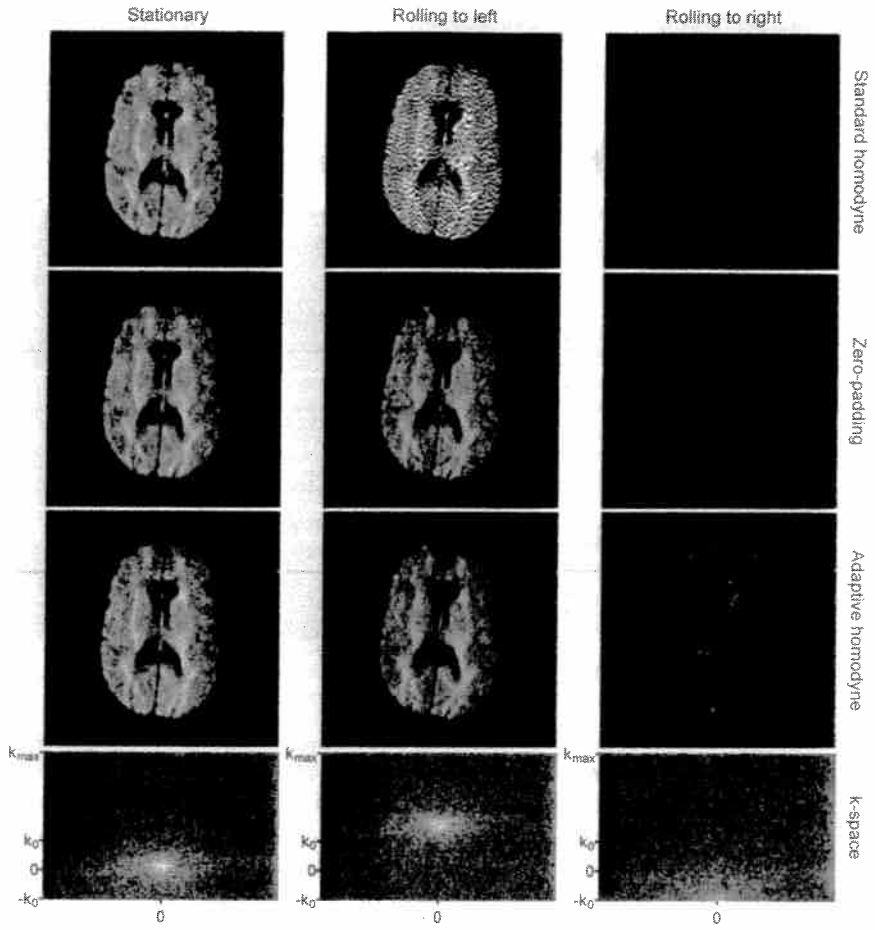

FIG. 3. Diffusion-weighted echo planar images images and the corresponding *k*-space data acquired from a healthy volunteer. In each case the PE direction was A/P, and the diffusion-sensitizing gradients were applied in the R/L direction. Results are shown with the subject holding his head stationary (first column), and rolling it gently to the left (second column) and right (third column). The top row shows the images obtained with standard homodyne reconstruction (the default method on GE scanners). The second and third rows show the images reconstructed retrospectively with zero-padding and the adaptive homodyne algorithm. The amplitudes of the raw data are displayed using a logarithmic intensity scale.

of the scanner bore. Images were acquired over a range of angular speeds ranging from 0.005 Hz (1.8° s^{-1}) to 0.1 Hz (36° s^{-1}). The direction of motion was varied, as were the FOV and the *b*-value. The remaining settings were identical to those used for the human studies, although the TE varied slightly with the FOV and *b*-value. For each set of acquisition parameters, the duration, separation, and amplitudes of the diffusion-sensitizing gradients were recorded to enable later comparison of the experimental results with theoretical predictions. Images were generated using standard homodyne reconstruction, and the raw data were saved. We calculated the phase images offline by zero-padding the raw data and evaluating the phase of the resulting complex image.

RESULTS

In the human studies, some of the images acquired during head motion exhibited signal loss or ripple-like intensity oscillations. The ripple artifacts were observed only on images acquired with the diffusion-sensitizing gradients in the frequency-encoding (R/L) direction, and occurred only when the subject rolled his head to the left. Signal loss was observed when he rolled his head to the right at similar speeds. Examples are shown in the top row of Fig. 3 (standard homodyne reconstruction).

The bottom row of the same figure shows the raw *k*-space data. Note that only a narrow band of negative k_y lines is sampled, and that the echo occurs at $\mathbf{k} = 0$ when the subject is stationary. When the subject rolls his head to the left, the raw data are displaced along the PE direction into the high-spatial-frequency range $[k_0, k_{max}]$. When he rolls his head to the right, the raw data increase in amplitude toward the bottom center of *k*-space, suggesting that the echo has been displaced outside the sampling range in the negative k_y direction.

The second row of Fig. 3 shows images reconstructed retrospectively with zero-padding. Note that the ripple artifacts are eliminated (center column). There is a slight loss of resolution in this image because some of the high-spatial-frequency components are shifted outside the *k*-space sampling range as the echo is displaced upwards. However, the stationary image (first column) exhibits a far greater loss of resolution. This is due to the omission of most of the negative *k*-space data. With motion to the right (third column), only the outlines of the brain structures are faintly visible. The DC component of the signal is absent because the center of the echo has been displaced outside the *k*-space sampling range. The remaining signal originates from high-spatial-frequency components of the image. The fact they are visible with zero-padding but not with standard homodyne reconstruction may be due to the fact that the weighting function used in the standard homodyne method (Fig. 1) suppresses data near the negative edge of *k*-space.

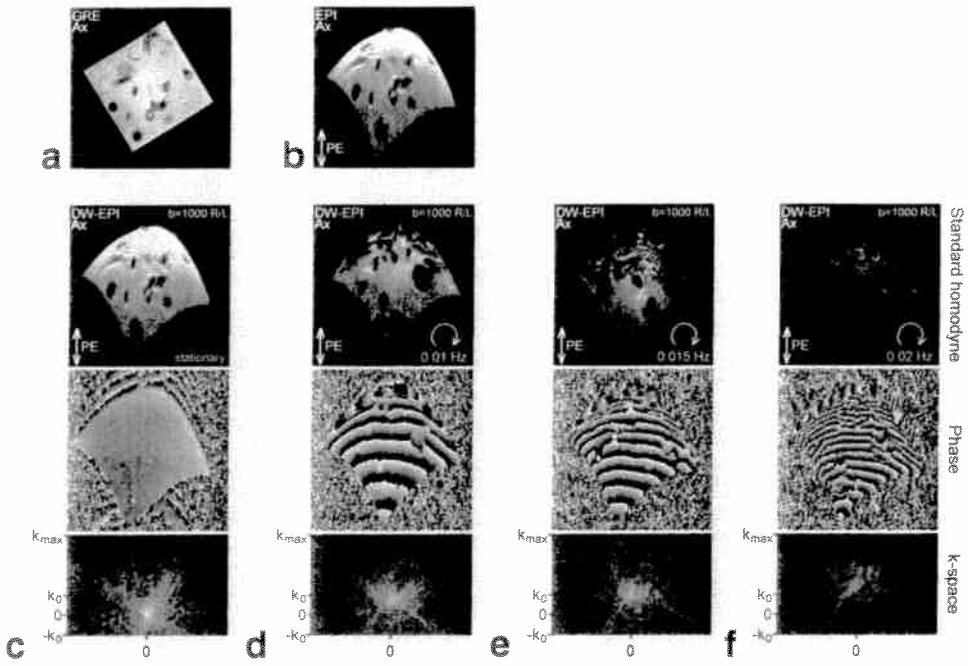

FIG. 4. Top row: Images of the phantom obtained with a gradient-echo (GRE) sequence (**a**) and an EPI sequence (**b**). The position of the phantom is the same in each. Bottom row: Diffusion-weighted echo planar images images and the corresponding phase images and *k*-space data acquired with the phantom stationary (**c**) and rotating at progressively higher speeds (**d–f**). Due to the motion, the position of the phantom is not identical among the images (**c–f**). The FOV was 20 cm for all acquisitions. The *b*-value is shown in units of s/mm^2.

The third row of Fig. 3 shows the images obtained with the adaptive homodyne method (illustrated in Fig. 2). Note that the ripple artifacts are eliminated and there is no loss of resolution in the stationary image. With motion to the right, the DC component of the signal is absent. The outlines of brain structures are visible, and are brighter than with zero-padding. This may be due to the modified weighting function used in the adaptive algorithm.

While the human studies confirmed the theory in a qualitative manner, they did not provide a quantitative test of Eq. [8], since it was not possible to measure the rotational velocity of the subject's head. This was the purpose of the phantom experiments. The phantom studies also offered us an opportunity to observe the effect of image distortion on the motion sensitivity. The distortion introduced by the echo planar readout is evident in Fig. 4 (compare a and b), and can be explained by the nonspherical shape of the phantom and the high field strength.

When the phantom was rotated with a positive angular velocity (equivalent to rolling the head to the left), ripple artifacts were observed on images with diffusion weighting in the R/L direction. At low rotational speeds the artifacts occurred only near the top of the phantom, where the image was compressed (Fig. 4d), but as the speed was increased the artifacts gradually covered more of the phantom (Fig. 4e). At even higher speeds the signal started to disappear, beginning at the top of the phantom (Fig. 4f).

The phase images provided direct visualization of the motion-induced phase shifts. In the stationary case the phase was fairly uniform across the phantom. (Note, however, some N/2 ghosting.) Rotational motion produced a phase shift across the image, which was nonlinear due to image distortion. The phase gradient was higher near the top of the phantom, where the image was compressed, than near the bottom of the phantom, where it was stretched out. As the rotational speed was incremented, the phase gradient increased throughout the phantom. In *k*-space, the higher speeds were associated with a greater shift of the raw data and a broadening of the echo. The echo-broadening reflects the distortion-related nonlinearity of the phase shift across the image.

The rotational speed of the phantom at which the artifacts appeared agreed with the theoretical predictions to within the accuracy of the measurements. With a *b*-value of 1000 s/mm^2, the gradient parameters were $G = 39.4$ mT/m, $\delta_{dur} = 21.1$ ms, and $\Delta_{sep} = 27.4$ ms. For a 20-cm FOV (giving $k_0 = 80$ m^{-1}), the theory predicted that artifacts should appear in regions of minimal distortion at a rotational speed of 0.0132 Hz (4.75° s^{-1}). Observations showed that at 0.010 Hz the artifacts were confined to the top of the phantom (Fig. 3d), but at 0.015 Hz they covered the center of the phantom (Fig. 3e). When the phantom was rotated at similar speeds in the opposite direction, the images exhibited signal loss. At −0.010 Hz only the top of the phantom was affected, and at −0.020 Hz the signal had disappeared almost completely throughout the entire image (data not shown).

When the FOV was increased (thereby reducing the value of k_0), the artifacts were observed at lower rotational speeds, in agreement with theory. Similarly, when the *b*-value was reduced (thereby decreasing δ_{dur} and Δ_{sep}), higher rotational speeds were needed to produce the artifacts. In regions of minimal distortion, the speeds at which the artifacts appeared were consistent in all cases with Eq. [8].

DISCUSSION

In diffusion imaging, rigid-body rotational motion introduces a phase gradient across the tissue, which is equivalent to a displacement of the echo in *k*-space. The displacement is orthogonal to both the axis of rotation and the direction of the diffusion-sensitizing gradients. If the DC component of the data is displaced outside the *k*-space sampling range, dramatic signal loss ensues. Partial *k*-space acquisitions increase the sensitivity of the technique

to motion since only the central range of *k*-space is fully sampled. For typical scanning parameters and 5/8 sampling, rotational velocities as low as ~4° s^{-1} are sufficient to displace the echo outside the central *k*-space range. If the displacement is negative, signal loss results, whereas if it is positive the conventional homodyne reconstruction algorithm fails, causing ripple-like intensity oscillations in the image. The intensity oscillations reflect the failure of the homodyne algorithm to treat correctly the rapid phase variation across the tissue.

The use of zero-padding instead of standard homodyne reconstruction eliminates the ripple artifacts but compromises the image resolution and may introduce truncation artifacts. As an alternative, we have implemented an adaptive version of the homodyne algorithm that dynamically adjusts the center and width of the homodyne filters according to the position of the echo. This method eliminates ripple artifacts in the presence of rigid-body motion and reduces to the standard homodyne algorithm in the absence of motion, thereby maintaining optimal image resolution. It cannot, however, recover signal that is lost when the echo is displaced outside the *k*-space sampling range. Furthermore, the adaptive method may perform poorly in situations of non-rigid-body motion, such as occurs in abdominal imaging. To address these problems it may be preferable to use full *k*-space sampling and minimize the TE by other means, such as parallel imaging.

ACKNOWLEDGMENTS

This project was supported in part by grants from the Ontario Research and Development Challenge Fund and the Natural Sciences and Engineering Research Council of Canada (to S.J.G.). P.S. is grateful to Yufen Chen, M.S., and Andres Carrillo, Ph.D., for their assistance.

REFERENCES

1. Stejskal EO, Tanner JE. Spin diffusion measurements: spin echoes in the presence of a time-dependent field gradient. J Chem Phys 1965;42:288–292.
2. Turner R, Le Bihan D, Chesnick AS. Echo-planar imaging of diffusion and perfusion. Magn Reson Med 1991;19:247–253.
3. Xu D, Henry RG, Mukherjee P, Carvajal L, Miller SP, Barkovich AJ, Vigneron DB. Single-shot fast spin-echo diffusion tensor imaging of the brain and spine with head and phased array coils at 1.5 T and 3.0 T. Magn Reson Imaging 2004;22:751–759.
4. Trouard TP, Sabharwal Y, Altbach MI, Gmitro AF. Analysis and comparison of motion-correction techniques in diffusion-weighted imaging. J Magn Reson Imaging 1996;6:925–935.
5. Norris DG. Implications of bulk motion for diffusion-weighted imaging experiments: effects, mechanisms and solutions. J Magn Reson Imaging 2001;13:486–495.
6. Wedeen VJ, Weisskoff RM, Poncelet BP. MRI signal void due to in-plane motion is all-or-none. Magn Res Med. 1994;32:116–120.
7. Noll DC, Nishimura DG. Homodyne detection in MRI. IEEE Trans Med Imaging 1991;10:154–163.
8. McGibney G, Smith MR, Nichols ST, Crawley A. Quantitative evaluation of several partial Fourier reconstruction algorithms used in MRI. Magn Reson Med 1993;30:51–59.
9. Reese TG, Heid O, Weisskoff RM, Wedeen VJ. Reduction of eddy-current-induced distortion in diffusion MRI using a twice-refocused spin echo. Magn Reson Med 2003;49:177–182.
10. Marmurek J, Baker N, Leung G, Wright GA, Plewes DB, Graham SJ. Retrospective correction of motion artifact in *k*-space using optical tracking. In: Proceedings of the 13th Annual Meeting of ISMRM, Miami Beach, FL, USA, 2005 (Abstract 2243).